ADVANCED FUNCTIONAL MATERIALS
www.afm-journal.de

Highly Stable Ion-Exchange Doping of Organic Semiconductor Single Crystals for Reliable Flexible Sensors

Tomohiro Murata, Yoshihisa Usami, Akiko Tajima, Tatsuyuki Makita, Yu Yamashita,* and Jun Takeya**

Thin-film single crystals of organic semiconductors represent a emerging class of materials for flexible printed electronic devices, including organic field-effect transistors and strain sensors. Their potential arises from the demonstration of high-mobility band transport, which significantly enhances both device performance and operational reliability. However, achieving stable and precise control over carrier concentration through chemical doping remains a fundamental challenge, restricting device architecture and broader application. In this study, the challenge is addressed by improving the environmental and thermal stability of chemically doped organic single crystals through the strategic selection of dopant anions. Specifically, ion-exchange doping using the bulky tetrakis(3,5-bis(trifluoromethyl) phenyl)borate (BArF) anion resulted in high electrical conductivity and exceptional stability under ambient conditions at 80 °C. The doped single crystals further exhibited excellent strain sensitivity, maintaining consistent strain sensing performance over 100 000 bending cycles, with conductivity drift suppressed to the order of ppm per hour under ambient conditions. These results highlight the importance of dopant ion design for stabilizing the doped state of organic semiconductors under environmental stress, without compromising mechanical flexibility or electronic functionality. This approach paves the way for robust and reliable flexible organic electronic devices.

1. Introduction

Thin-film single crystals of organic semiconductors (OSCs) offer unique opportunities for the development of advanced solution-processed electronic devices, including field-effect transistors,[1,2] light-emitting diodes,[3,4] and sensors.[5–7] Carrier transport in OSCs is governed by their π-conjugated system, where 2D molecular packing of the conjugated cores enables high-mobility (>10 $cm^2 V^{-1} s^{-1}$) band transport.[8–10] Recent advances in molecular design and solution-based processing have enabled the fabrication of large-area organic single crystals with improved solubility and high carrier mobility,[2,11] paving the way for integrated circuits capable of operating in the tens of megahertz range and beyond.[12] To fully exploit the potential of these materials, doping processes that adjust conductivity after crystal growth are of critical importance.[13–15] Doping in organic semiconductors (OSCs) is achieved by introducing impurity molecules that exchange electrons with the π-conjugated system.[16–18] To avoid disrupting the highly ordered structure of OSC single crystals, carrier concentration can be modulated by forming a dopant or ionic layer exclusively on the crystal surface.[19,20] The resulting doped single crystals retain coherent charge transport, which is essential for achieving reliable and reproducible responses in sensing applications.[21]

Band transport in the soft lattices of OSC single crystals offers a foundation for a variety of applications, among which the development of reliable mechanical sensors is a notable example. The charge-carrier mobility in OSCs is strongly influenced by molecular vibrations within their soft crystal lattices, which are formed by weak van der Waals interactions.[22,23] Owing to these weak intermolecular interactions, the mobility is highly sensitive to mechanical stress, which modulates the amplitude of molecular vibrations.[24] These characteristics make OSC single crystals attractive for use in strain sensors, which detect mechanical deformation and convert it into electrical signals. Strain sensors are critical components in a wide range of applications, including structural monitoring and biomedical systems. Their integration into wearable electronics has attracted significant attention, particularly for applications in health monitoring and human motion analysis.[25–27] Furthermore, the sensitive detection

T. Murata, Y. Usami, A. Tajima, Y. Yamashita, J. Takeya
Department of Advanced Materials Science
Graduate School of Frontier Sciences
The University of Tokyo
5-1-5 Kashiwanoha, Kashiwa, Chiba 277-0882, Japan
E-mail: tmurata@edu.k.u-tokyo.ac.jp; YAMASHITA.Yu@nims.go.jp; takeya@k.u-tokyo.ac.jp

T. Makita, J. Takeya
Pi-Crystal Inc
273-1 Kashiwa, Kashiwa, Chiba 277-0005, Japan

Y. Yamashita, J. Takeya
Research Center for Materials Nanoarchitectonics
National Institute for Material Science (NIMS)
1-1 Namiki, Tsukuba, Ibaraki 305-0044, Japan

The ORCID identification number(s) for the author(s) of this article can be found under https://doi.org/10.1002/adfm.202518055

DOI: 10.1002/adfm.202518055

of mechanical strain is fundamental to the development of label-free chemomechanical sensors that detect molecular adsorption and related phenomena, including biosensing, gas detection, and chemical reactions.[28–30]

The ability to control carrier concentration in OSC single crystals is a key requirement for unlocking their potential across a wide spectrum of advanced organic electronic devices. For the fabrication of readily measurable two-terminal resistive sensors, chemical doping via redox reactions has been employed to introduce carriers at the surface of OSC single crystals.[19,31] Maintaining a high doping level is essential for achieving band transport through effective trap filling, which can contribute to the reduction of electronic noise.[32] However, achieving stable doping levels remains a critical challenge, since doped OSCs gradually degrade through interactions with atmospheric species such as water and oxygen. To improve the stability of the doped state in OSCs, the choice of dopant ions plays a key role.[33,34] In particular, reduction of p-type doped OSCs by atmospheric water can lead to decreased doping levels and a drop in conductivity.[35,36] Differences in anion hygroscopicity alter the interactions with water, thereby influencing doping stability.[37,38] These findings suggest that the proper design of dopant anions may offer a route to enhance the ambient stability of doped OSCs. However, most prior studies have focused on polymeric semiconductors, in which both holes and anions are distributed throughout the bulk. The specific impact of dopant anions on doping stability in surface-doped OSC single crystals remains unclear.

In this study, we demonstrated that the degradation of the doped state in organic single crystals was significantly suppressed through our selection of dopant molecules and the design of the device structure. This approach enhances the long-term performance of strain sensors and facilitates the development of more reliable and practical organic electronic devices.

2. Results and Discussion

The schematic structure of our device is shown in **Figure 1a**. Our benchmarked organic single crystal, 3,11-dinonyldinaphtho[2,3-*d*:2',3'-*d*']benzo[1,2-*b*:4,5-*b*']dithiophene (C9-DNBDT-NW, Figure 1b),[11,39] was deposited using a meniscus-guided solution process. Details of the process are described elsewhere.[2,11,40] The lower parylene layer is used to improve wettability for making the OSC film on a polyimide flexible substrate. The formation and quality of the OSC film were confirmed by cross-polarized optical microscopy, as shown in Figure 1c. Variations of brightness were observed between the gold electrodes, which are attributed to differences in film thickness and indicate the formation of molecular step terraces of the single crystal.[2] The dopant layer consists of an oxidant 2,3,5,6-tetrafluoro-7,7,8,8-tetracyano-quinodimethane (F_4TCNQ), a salt for ion exchange, and polymethyl methacrylate (PMMA). Two types of salts, cesium(I) bis(trifluoromethanesulfonyl)imide (CsTFSI) and sodium tetrakis[3,5-bis(trifluoromethyl)phenyl]borate (NaBArF), were used for the ion exchange (Figure 1b). The oxidant extracts electrons from the OSC single crystal, generating an ion pair [$OSC^{\bullet+}F_4TCNQ^{\bullet-}$]. This anion is then exchanged with other anions such as $TFSI^-$ or $BArF^-$, which are considered to bind to the surface of the single crystal, as illustrated in Figure 1a. The formation of [OSC^+TFSI^-] or [OSC^+BArF^-] leads to hole injection into OSC and contributes to the electrical conductivity. PMMA enables the formation of a uniform dopant layer, thereby serving to retain the dopant molecules, suppress their diffusion, and improve the reproducibility of the doping process.[31] A CYTOP coating is applied on top of the dopant layer to enhance barrier properties, followed by parylene and aluminum layers that serve as encapsulation layers.

The type of anion significantly influences the doping level. Figure 1d shows the variation in two-terminal sheet conductivity depending on the anion used for ion exchange. The two terminal sheet conductivity obtained using $BArF^-$ anions was approximately twice that achieved with $TFSI^-$ anions. This difference can be attributed to the ion affinities involved in the doping process.[33] To rule out the possibility that differences in channel quality, such as crystal orientation, affect the observed conductivity, we performed statistical measurements on doped samples. The average sheet conductivity of 20 independent devices was 5.7 ± 0.4 μS for $BArF^-$-doped samples and 2.1 ± 0.2 μS for $TFSI^-$-doped samples. This demonstrates that the higher conductivity of the $BArF^-$-doped crystals is attributed to the anion-dependent doping effect rather than variations in pristine crystal quality.

The difference of conductivity also influences the temperature dependence of conductivity, as shown in Figure S1 (Supporting Information). The $BArF^-$-doped sample exhibits a negative temperature coefficient, indicating a carrier density high enough to support band-like rather than hopping transport. Although negative temperature dependence of conductivity has been reported for $TFSI^-$-doped samples,[19] our $TFSI^-$-doped sample shows a positive dependence. A likely cause of this discrepancy is the doping environment: unlike previous studies conducted under nitrogen, our doping was performed under ambient air, where water molecules may have interacted with and degraded the doped state, possibly introduced carrier traps that resulted in hopping-dominated transport behavior. Indeed, the resulting conductivity was approximately half of the value reported in previous studies. In contrast, $BArF^-$ doping yielded band-like temperature dependence even under ambient conditions, demonstrating that stable band transport can be achieved without the need for a strictly inert atmosphere. This robustness offers a practical advantage for scalable manufacturing processes.

To investigate the stability of the doping state, we applied thermal stress and monitored the changes of sheet conductivity over time. Samples were heated at various temperatures on a hot plate, and their time-dependent conductivities were measured. Normalized changes in conductivities are shown in **Figure 2**. In the case of doping with the TFSI anion, a progressive decrease in conductivity was observed with increasing temperature. On the other hand, for doping with the BArF anion, almost no degradation of conductivity was observed up to 80°C. A comparison of conductivity changes after 600 hours reveals that TFSI doping results in variations of −4.7, − 23, − 49, − 62% at 40, 60, 80, and 100 °C, respectively, whereas BArF doping shows changes of −1.3, 2.5, − 2.3, − 40%, indicating that conductivity degradation is significantly suppressed at all temperatures except at 100 °C. The degradation of the doped state is attributed to factors such as dopant diffusion and the influence of water molecules.[35,41] At 100 °C, significant degradation was observed in both samples.

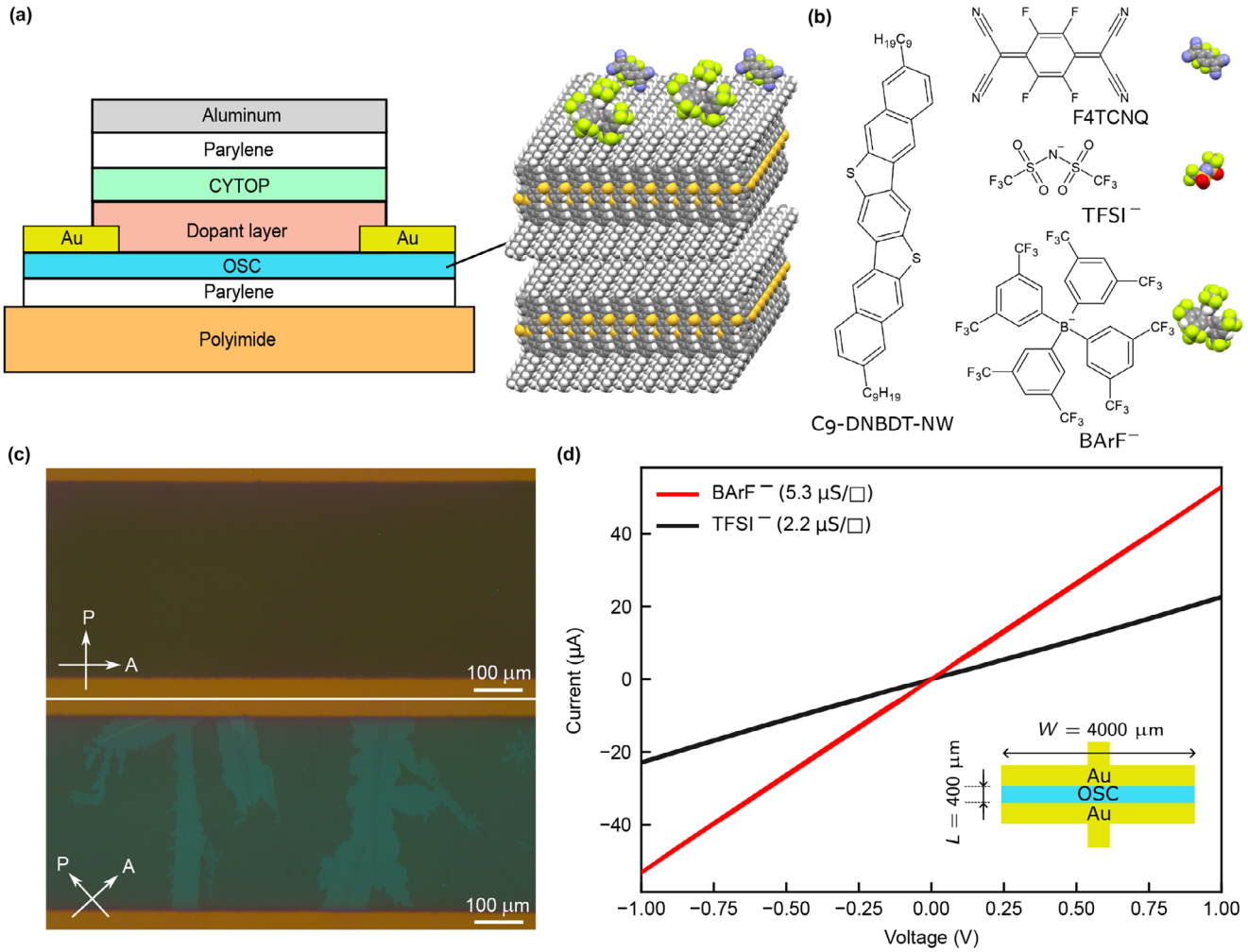

Figure 1. Structural and electrical characterization of the organic strain sensor. a) Cross-sectional schematic structure of the fabricated strain sensor with the crystal structure of the organic semiconductor C9-DNBDT-NW. Approximate thicknesses of each layer are as follows: 100 and 500 nm for lower and upper parylene layers, 10 nm for OSC layer, 300 nm for the dopant layer, 100 nm for CYTOP layer, and 100 nm for aluminum layer. b) Chemical structures of the dopant, anions, and the organic semiconductor. c) Cross-polarized optical microscopy images of the coated organic semiconductor film. d) Comparison of the I–V characteristics after doping with $BArF^-$ and $TFSI^-$ anions.

This degradation may be attributed to the glass transition of PMMA, accelerating the transport of water and/or dopants.

The thermal stability difference between the $TFSI^-$ anion and the $BArF^-$ anion can be ascribed to differences in hygroscopicity. In p-type doping, one of the primary causes of doped state degradation is the presence of water.[41] The $BArF^-$ molecule is a much bulkier and more hydrophobic anion than $TFSI^-$, which effectively mitigates degradation mechanisms such as dopant diffusion and moisture-induced reactions. To verify the difference in hygroscopicity between the two dopant layers, surface contact angles were measured (**Figure 3a**). The sample coated with F_4TCNQ/NaBArF/PMMA exhibited a significantly higher contact angle than that with F_4TCNQ/CsTFSI/PMMA. The contact angle of F_4TCNQ/PMMA was nearly identical to that of the F_4TCNQ/CsTFSI/PMMA layer (Figure S2, Supporting Information). Although the present device structure includes multiple sealing layers to prevent moisture ingress, additional sealing is often impractical in flexible devices due to limitations in mechanical compliance. Therefore, the intrinsic hydrophobicity of the dopant layer becomes a key factor in ensuring environmental stability.

To further evaluate the effects of anion type and sealing on moisture-induced degradation, thermal cycling tests were conducted under controlled humidity conditions. Since molecular diffusion accelerates with temperature, cycling the devices between 25 °C and 80 °C at a constant 50% relative humidity (RH) provides a stringent test for dopant stability. We monitored conductivity over time to assess the environmental robustness of the doped state.

As shown in Figure 3b, sealing plays a critical role in suppressing conductivity degradation during thermal cycling. Unsealed $BArF^-$-doped samples, despite exhibiting surface hydrophobicity, showed a monotonic decline in conductivity under repeated stress. In contrast, sealed $BArF^-$-doped devices exhibited only a transient increase in conductivity during the initial cycles and remained stable under harsh conditions of 80 °C and 50% RH.

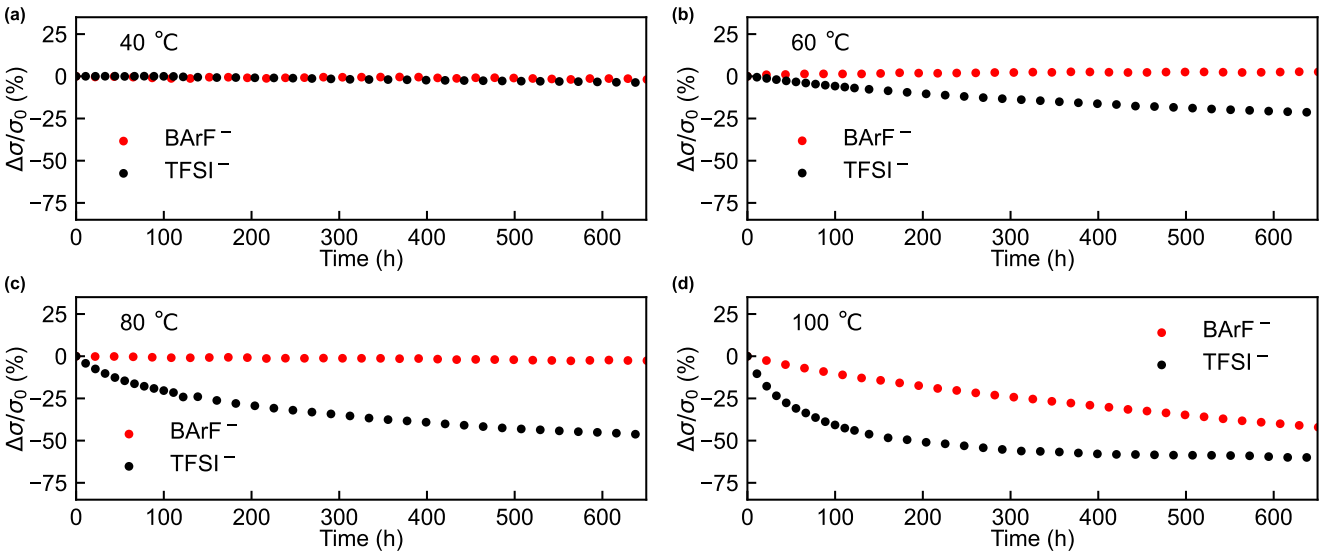

Figure 2. Long-term conductivity stability of $BArF^-$ and $TFSI^-$ doped samples during air exposure at elevated temperatures: a) 40 °C, b) 60 °C, c) 80 °C, and d) 100 °C.

For $TFSI^-$-doped samples, even sealed devices exhibited a conductivity decrease of approximately 15% within 24 hours over five thermal cycles, with further degradation observed upon continued cycling. Unsealed $TFSI^-$ samples degraded even more rapidly. These results indicate that sealing is essential to suppress environmental degradation, but the choice of anion is also crucial. The $BArF^-$ anion renders the surface hydrophobic, and in combination with sealing, effectively prevents water ingress. This dual protection helps suppress conductivity loss under high-temperature and high-humidity conditions, highlighting the importance of moisture resistance in achieving long-term doped-state stability.

Interestingly, in Figure 3b, $TFSI^-$-doped samples exhibit conductivity decreases upon heating, which contrasts with the positive temperature dependence of conductivity observed in Figure S1 (Supporting Information) attributed to hopping transport. This discrepancy is likely due to swelling of the polyimide substrate caused by water uptake under 50% RH, inducing strain in the OSC layer. The direction of strain–tensile or compressive–may vary depending on surface morphology of the substrate. The consistent monotonic degradation observed in both unsealed $BArF^-$- and all $TFSI^-$-doped devices over repeated thermal stress suggests that the long-term degradation is caused by doped-state instability.

The response to the strain of the device, which achieved a high stable doped state using the $BArF^-$ anion, was tested. The large strain response observed in OSC single crystals is attributed to carrier transport influenced by molecular vibrations,[24] which is

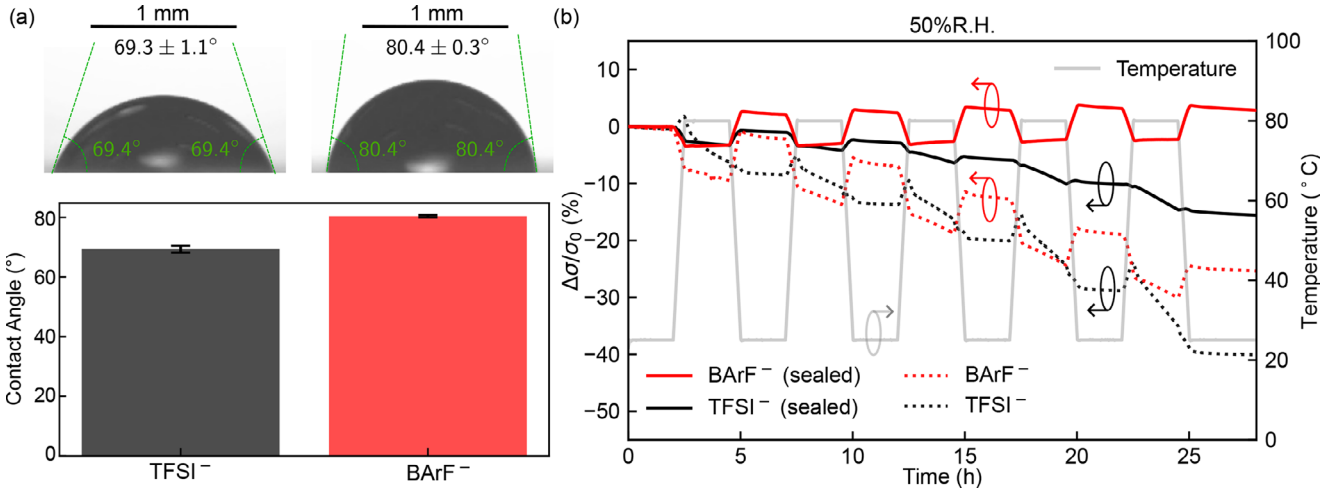

Figure 3. Stability under repeated thermal stress and contact angle measurements of $BArF^-$ and $TFSI^-$ doped samples. a) Comparison of contact angles for the surface of $BArF^-$ and $TFSI^-$ doped samples (n=3). b) Thermal cycling test of samples doped with $BArF^-$ and $TFSI^-$ anions under controlled 50% relative humidity. Solid lines represent sealed samples (CYTOP, parylene, and Al), while dotted plots indicate unsealed samples.

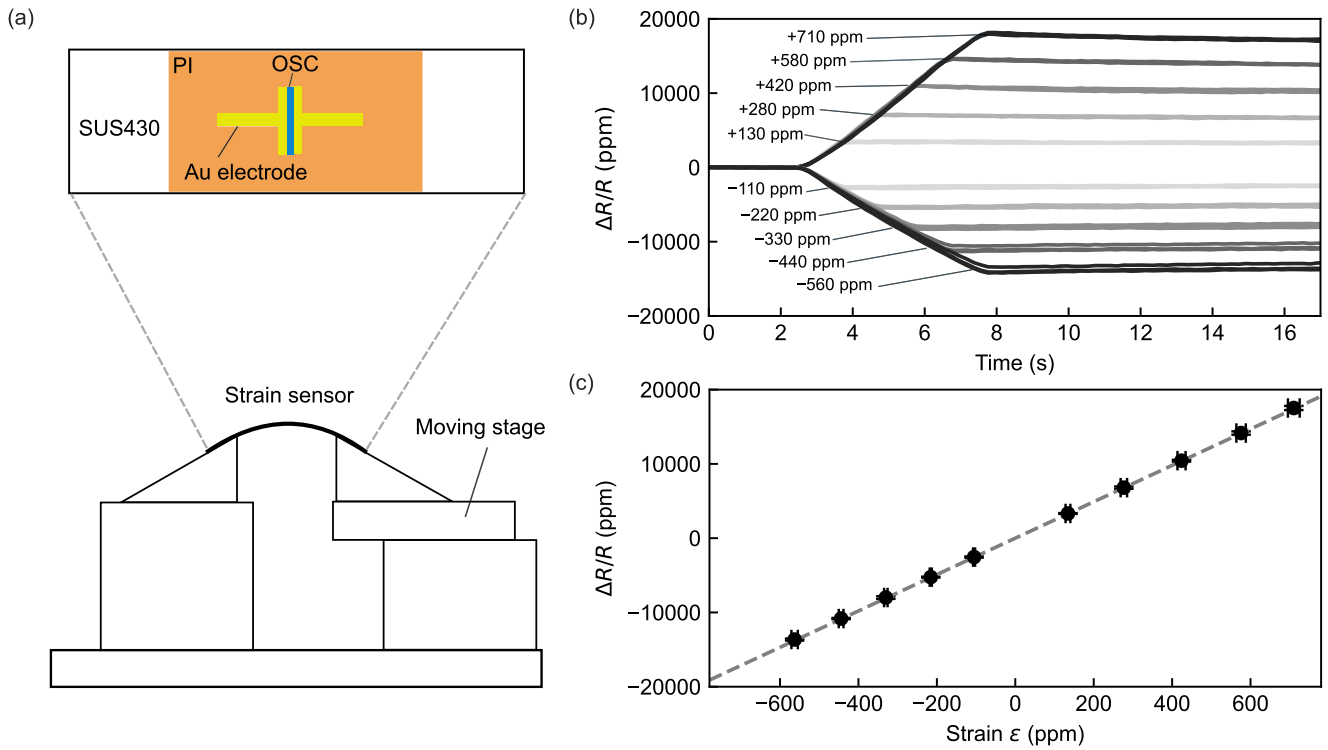

Figure 4. Performance of the BArF-doped device as the strain sensor. a) Schematic illustration for the strain test setup. b) Sensor responses to the elevated mechanical strain applied in both positive and negative directions. Each strain level was applied three times. c) Plot of applied mechanical strain versus resistance change, used to evaluate the gauge factor of the $BArF^-$ doped device.

unique to the crystal structure. Previous studies on chemically doped organic single crystals strongly suggest that the dopant species remain at the crystal surface rather than being incorporated into the lattice,[19] but it is not obvious whether the presence of bulky anions influences the strain response originating from molecular vibrations. To evaluate this, we prepared a setup as shown in **Figure** 4a, where controlled strain was applied to the doped sensor device, and its resistance response to strain was measured.

Figure 4b shows the resistance change when strain was applied, with three cycles of strain application overlaid in the graph. Examining the relationship between strain and resistance change rate, a clear linear response was observed for both positive and negative strain, as shown in Figure 4c. The gauge factor, defined as the ratio of resistance change to applied strain, was found to be as high as 24 (Figure 4c). Previous studies on pristine OSC single crystals, where charge carriers were induced electrostatically via gate electrodes, have demonstrated comparable strain sensitivities.[24] In this work, we show that chemical doping enables a similar level of strain sensitivity without the need for external gating, thereby simplifying the device structure and facilitating practical applications. These results indicate that even with the introduction of bulky anions via surface chemical doping, the strain response was not disturbed, and a linear strain response was maintained. The value of the gauge factor observed in the OSC is approximately 10 times higher than that of typical nichrome strain gauges.[42,43] Higher gauge factors have been reported for crack-assisted architectures, such as aligned CNT/elastomer composites (GF≈200[44]) and MXene-based sensors (GF≈500[45]). Such values, however, typically rely on domain-separation mechanisms that lead to nonlinear and asymmetric responses for positive and negative strain. By contrast, our chemically doped organic single-crystal devices exhibit GF≈20, while maintaining linear and symmetric responses to both tensile and compressive deformation. These features not only highlight their advantage for sensitive detection of ppm-level deformations but also position our devices as a unique and practical platform for stable, reproducible, and low-cost strain sensing enabled by scalable solution-coating processes. A summary of representative resistive strain-sensor performances, including gauge factors in the small-strain regime (<1%), is provided in Table S1 (Supporting Information).

Next, we repeatedly applied a constant strain of approximately 300 ppm under ambient conditions for a total of 100 000 cycles to investigate whether the resistance change rate varied over time. **Figure** 5a displays the resistance changes during the first 20 cycles, while Figure 5b presents the overlaid responses from all 100 000 strain cycles. As shown in Figure 5c, a stable and reproducible resistance change was observed in response to constant strain, confirming that the strain response remained stable despite repeated strain application. These findings suggest that the deposition of bulky anions on the single-crystal surface does not impair carrier conduction and is highly effective in achieving a stable doped state.

The baseline resistance drift observed in Figure 5b was approximately 20 ppm/h over a 50-hour measurement period under ambient conditions. This level of temporal stability is considered sufficient for reliable detection of ppm-scale strain signals.

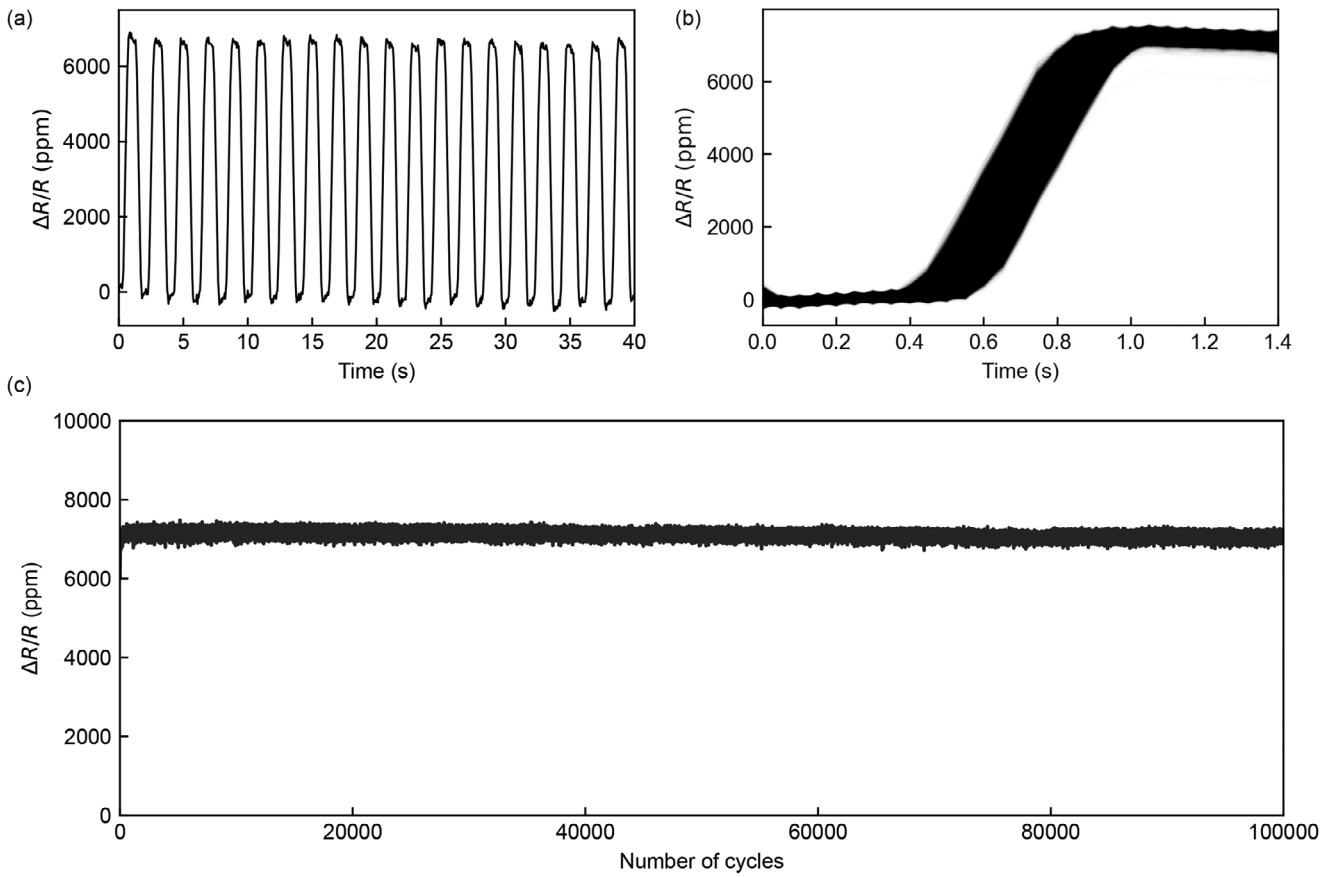

Figure 5. Stability of the BArF-doped strain sensor under repeated strain cycles, tested under ambient conditions. a) Sensor output during the first 20 cycles of applied strain. b) Overlay of all output signals over the 100 000 strain cycles. c) Stability of sensor signals versus strain cycles.

Despite the limited number of studies on the long-term stability of surface-doped organic single crystals, C9-DNBDT-NW doped with $TFSI^-$ has been reported to drift at a rate of 50 ppm/h under ambient conditions. The present strategy suppresses this drift to well below half that level. Moreover, it offers a pronounced advantage over TFSI-doping in mitigating conductivity loss at elevated temperatures (Figure 2). Further decrease in drift and detection of smaller strain may be attainable by the implementation of appropriate drift compensation techniques.[46–48]

3. Conclusion

This study highlights the critical role of anion selection in governing the stability and performance of doped organic single crystals under mechanical and thermal stress. Compared to the conventional use of $TFSI^-$ anion, employing $BArF^-$ anion resulted in improved stability under ambient conditions and at elevated temperatures. Our results indicate that moisture accelerates conductivity degradation, highlighting the role of low hygroscopicity of BArF molecule in enhancing durability. Contact angle measurements further confirmed the low hygroscopicity of the BArF-containing dopant layers. The single crystal doped with $BArF^-$ anion retained its intrinsic strain responsiveness even under repeated strain cycles, demonstrating mechanical durability. These results demonstrate that DNBDT single crystals doped with $BArF^-$ anion are well-suited for detecting minute strain at the ppm level. This study offers valuable insights into overcoming challenges related to doped-state degradation and structural instability, paving the way for the development of robust organic electronic devices with enhanced functionality and long-term performance.

4. Experimental Section

Fabrication of Device: A 16 µm thick polyimide film (Toray-Dupont) was used as the substrate. A 100 nm thick parylene layer was deposited onto the substrate to enhance the coating properties of the OSC single crystal. The benchmark material, 3,11-dinonyl-dinaphtho[2,3-d:2',3'-d']benzo[1,2-b:4,5-b']dithiophene (C9-DNBDT-NW), was coated onto the parylene layer using a continuous edge-casting method. The film was subsequently annealed at 80 °C under vacuum overnight. Photolithography was used to pattern both the OSC film and the gold electrodes in order to prevent unintended electrical connections. The dopant solution, prepared under a nitrogen atmosphere, consisted of 10 mM CsTFSI or NaBArF, 10 mM F_4TCNQ as the oxidant, and 2 wt% PMMA in 2,2,2-trifluoroethanol. The solution was spin-coated on the OSC film at 2000 rpm for 60 seconds under ambient conditions to form the dopant layer. This layer was subsequently heated at 120 °C for 30 min to remove the solvent. A protective layer consisting of CYTOP, parylene, and aluminum layers was subsequently applied. The CYTOP layer was formed by spin-coating a fivefold-diluted CYTOP 809 M solution at 2000 rpm, followed by heating at 120 °C for 30 min to improve adhesion. An approximately 500 nm thick parylene

layer was introduced to mitigate damage from the subsequent aluminum deposition. The aluminum layer, with a thickness of 100 nm, was deposited by thermal evaporation using a shadow mask.

Electrical Measurements: Silver paste (DOTITE D-550, FUJIKURA KASEI) was used for electrical contact with the gold electrodes. For temperature-dependent time measurements, a hot plate and a data logger (DAQ970A, KEYSIGHT) were employed. An environmental test chamber (SH-222, ESPEC) was utilized for temperature tests under controlled humidity.

To apply strain, the device on the polyimide film was affixed to 100 µm of SUS430 substrate and secured in an arched configuration. Strain was induced by bending this arched structure through the movement of a moving stage (OSMS26-200, OptoSigma). The moving stage was controlled by a stage controller (SHOT-302GS, OptoSigma). The relationship between stage displacement and strain was calibrated using a commercially available strain sensor with a known gauge factor (KFGS-1-120-C1-11 L1M2R, Kyowa). A 1.5 V bias from a DC power supply (PMX18-2A, KIKUSUI) was applied to the OSC single crystal, with an 80 kΩ resistor connected in series, and the voltage across the OSC single-crystal device was monitored. Voltage measurements were conducted using an analog-to-digital converter (AD7148-8, Analog Devices) and its evaluation kit. All strain application experiments were performed at room temperature.

Supporting Information

Supporting Information is available from the Wiley Online Library or from the author.

Acknowledgements

This work was supported in part by JSPS KAKENHI grant (JP22H04959), JST CREST (JPMJCR21O3), and JST FOREST (JPMJFR236R).

Conflict of Interest

The authors declare no conflict of interest.

Data Availability Statement

The data that support the findings of this study are available from the corresponding author upon reasonable request.

Keywords

molecular doping, organic semiconductor, single crystals, strain sensor

Received: July 14, 2025
Revised: August 25, 2025
Published online: September 19, 2025

[1] K. Myny, S. Steudel, S. Smout, P. Vicca, F. Furthner, B. Van Der Putten, A. Tripathi, G. Gelinck, J. Genoe, W. Dehaene, *Org. Electron.* **2010**, *11*, 1176.
[2] A. Yamamura, S. Watanabe, M. Uno, M. Mitani, C. Mitsui, J. Tsurumi, N. Isahaya, Y. Kanaoka, T. Okamoto, J. Takeya, *Sci. Adv.* **2018**, *4*, eaao5758.
[3] J. Liu, H. Zhang, H. Dong, L. Meng, L. Jiang, L. Jiang, Y. Wang, J. Yu, Y. Sun, W. Hu, A. J. Heeger, *Nat. Commun.* **2015**, *6*, 10032.
[4] R. Ding, J. Feng, F. Dong, W. Zhou, Y. Liu, X. Zhang, X. Wang, H. Fang, B. Xu, X. Li, H. Wang, S. Hotta, H. Sun, *Adv. Funct. Mater.* **2017**, *27*, 1604659.
[5] H. U. Khan, M. E. Roberts, O. Johnson, R. Förch, W. Knoll, Z. Bao, *Adv. Mater.* **2010**, *22*, 4452.
[6] P. Lin, F. Yan, *Adv. Mater.* **2012**, *24*, 34.
[7] B. Peng, S. Huang, Z. Zhou, P. K. L. Chan, *Adv. Funct. Mater.* **2017**, *27*, 1700999.
[8] J. Takeya, K. Tsukagoshi, Y. Aoyagi, T. Takenobu, Y. Iwasa, *Jpn. J. Appl. Phys.* **2005**, *44*, L1393.
[9] V. Podzorov, E. Menard, J. A. Rogers, M. E. Gershenson, *Phys. Rev. Lett.* **2005**, *95*, 226601.
[10] J. Tsurumi, H. Matsui, T. Kubo, R. Häusermann, C. Mitsui, T. Okamoto, S. Watanabe, J. Takeya, *Nat. Phys.* **2017**, *13*, 994.
[11] S. Kumagai, A. Yamamura, T. Makita, J. Tsurumi, Y. Y. Lim, T. Wakimoto, N. Isahaya, H. Nozawa, K. Sato, M. Mitani, T. Okamoto, S. Watanabe, J. Takeya, *Sci. Rep.* **2019**, *9*, 15897.
[12] A. Yamamura, T. Sakon, K. Takahira, T. Wakimoto, M. Sasaki, T. Okamoto, S. Watanabe, J. Takeya, *Adv. Funct. Mater.* **2020**, *30*, 1909501.
[13] B. Lüssem, C.-M. Keum, D. Kasemann, B. Naab, Z. Bao, K. Leo, *Chem. Rev.* **2016**, *116*, 13714.
[14] H. Jiang, W. Hu, *Angew. Chem., Int. Ed.* **2020**, *59*, 1408.
[15] X. Zhao, H. Zhang, J. Zhang, J. Liu, M. Lei, L. Jiang, *Adv. Sci.* **2023**, *10*, 2300483.
[16] P. Pingel, D. Neher, *Phys. Rev. B* **2013**, *87*, 115209.
[17] I. Salzmann, G. Heimel, M. Oehzelt, S. Winkler, N. Koch, *Acc. Chem. Res.* **2016**, *49*, 370.
[18] I. E. Jacobs, A. J. Moulé, *Adv. Mater.* **2017**, *29*, 1703063.
[19] S. Watanabe, R. Hakamatani, K. Yaegashi, Y. Yamashita, H. Nozawa, M. Sasaki, S. Kumagai, T. Okamoto, C. G. Tang, L. Chua, P. K. H. Ho, J. Takeya, *Adv. Sci.* **2021**, *8*, 2002065.
[20] N. Kasuya, J. Tsurumi, T. Okamoto, S. Watanabe, J. Takeya, *Nat. Mater.* **2021**, *20*, 1401.
[21] Y. Yamashita, H. Hayakawa, P. Wang, T. Makita, S. Kumagai, S. Watanabe, J. Takeya, *Proc. Natl. Acad. Sci. USA* **2024**, *121*, e2405933121.
[22] S. Fratini, M. Nikolka, A. Salleo, G. Schweicher, H. Sirringhaus, *Nat. Mater.* **2020**, *19*, 491.
[23] S. Fratini, D. Mayou, S. Ciuchi, *Adv. Funct. Mater.* **2016**, *26*, 2292.
[24] T. Kubo, R. Häusermann, J. Tsurumi, J. Soeda, Y. Okada, Y. Yamashita, N. Akamatsu, A. Shishido, C. Mitsui, T. Okamoto, S. Yanagisawa, H. Matsui, J. Takeya, *Nat. Commun.* **2016**, *7*, 11156.
[25] S. Choi, H. Lee, R. Ghaffari, T. Hyeon, D. Kim, *Adv. Mater.* **2016**, *28*, 4203.
[26] X. Wang, Z. Liu, T. Zhang, *Small* **2017**, *13*, 1602790.
[27] T. Yamada, Y. Hayamizu, Y. Yamamoto, Y. Yomogida, A. Izadi-Najafabadi, D. N. Futaba, K. Hata, *Nat. Nanotechnol.* **2011**, *6*, 296.
[28] J. Arlett, E. Myers, M. Roukes, *Nat. Nanotechnol.* **2011**, *6*, 203.
[29] G. Yoshikawa, T. Akiyama, S. Gautsch, P. Vettiger, H. Rohrer, *Nano Lett.* **2011**, *11*, 1044.
[30] J. Gimzewski, C. Gerber, E. Meyer, R. Schlittler, *Chem. Phys. Lett.* **1994**, *217*, 589.
[31] Y. Usami, Y. Yamashita, T. Murata, T. Matsumoto, M. Ito, S. Watanabe, J. Takeya, *Sci. Technol. Adv. Mater.* **2025**, *26*, 2451020.
[32] S. Watanabe, H. Sugawara, R. Häusermann, B. Blülle, A. Yamamura, T. Okamoto, J. Takeya, *Commun. Phys.* **2018**, *1*, 37.
[33] Y. Yamashita, J. Tsurumi, M. Ohno, R. Fujimoto, S. Kumagai, T. Kurosawa, T. Okamoto, J. Takeya, S. Watanabe, *Nature* **2019**, *572*, 634.
[34] E. M. Thomas, K. A. Peterson, A. H. Balzer, D. Rawlings, N. Stingelin, R. A. Segalman, M. L. Chabinyc, *Adv. Electron. Mater.* **2020**, *6*, 12.
[35] C. G. Tang, M. C. Ang, K.-K. Choo, V. Keerthi, J.-K. Tan, M. N. Syafiqah, T. Kugler, J. H. Burroughes, R.-Q. Png, L.-L. Chua, et al., *Nature* **2016**, *539*, 536.

[36] T. Kurosawa, Y. Yamashita, Y. Kobayashi, C. P. Yu, S. Kumagai, T. Mikie, I. Osaka, S. Watanabe, J. Takeya, T. Okamoto, *Macromolecules* **2023**, *57*, 328.
[37] C. G. Tang, M. N. Syafiqah, Q.-M. Koh, M. C.-Y. Ang, K.-K. Choo, M.-M. Sun, M. Callsen, Y.-P. Feng, L.-L. Chua, R.-Q. Png, P. K. H. Ho, *Nat. Commun.* **2023**, *14*, 3978.
[38] Q.-M. Koh, C. G. Tang, M. C.-Y. Ang, K.-K. Choo, Q.-J. Seah, R.-Q. Png, L.-L. Chua, P. K. Ho, *Nat. Commun.* **2021**, *12*, 3345.
[39] C. Mitsui, T. Okamoto, M. Yamagishi, J. Tsurumi, K. Yoshimoto, K. Nakahara, J. Soeda, Y. Hirose, H. Sato, A. Yamano, T. Uemura, J. Takeya, *Adv. Mater.* **2014**, *26*, 4546.
[40] J. Soeda, T. Uemura, T. Okamoto, C. Mitsui, M. Yamagishi, J. Takeya, *Appl. Phys. Express* **2013**, *6*, 076503.
[41] C. G. Tang, K. Hou, W. L. Leong, *Chem. Mater.* **2024**, *36*, 28.
[42] I. H. Kazi, P. Wild, T. Moore, M. Sayer, *Thin Solid Films* **2006**, *515*, 2602.
[43] W. Tillmann, D. Kokalj, D. Stangier, *Surf. Coat. Technol.* **2018**, *344*, 223.
[44] M. O. Tas, M. A. Baker, M. G. Masteghin, J. Bentz, K. Boxshall, V. Stolojan, *ACS Appl. Mater. Interfaces* **2019**, *11*, 39560.
[45] Y. Liu, Z. Xu, X. Ji, X. Xu, F. Chen, X. Pan, Z. Fu, Y. Chen, Z. Zhang, H. Liu, B. Cheng, J. Liang, *Nat. Commun.* **2024**, *15*, 5354.
[46] T. G. Thuruthel, B. Shih, C. Laschi, M. T. Tolley, *Sci. Rob.* **2019**, *4*, eaav1488.
[47] P. Vitolo, D. Pau, G. D. Licciardo, M. Pesaturo, S. Bosco, S. Pennino, in *2023 IEEE International Instrumentation and Measurement Technology Conference (I2MTC)*, IEEE, Kuala Lumpur, Malaysia, ISBN 978-1-6654-5383-7 **2023**, pp. 01–05.
[48] Y. Chen, C. Xu, X. Zhao, *Meas. Sci. Technol.* **2023**, *34*, 025107.